Geophysical Journal International

Royal Astronomical Society

Geophys. J. Int. (2025) **241**, 756–769 Advance Access publication 2025 February 21 GJI Seismology https://doi.org/10.1093/gji/ggaf072

Improving passive reflection seismic imaging in complex geological settings through site effect reduction: application to Krafla volcano, Iceland

Regina Maass[®], Ka Lok Li[®] and Christopher J Bean

Geophysics Section, Dublin Institute for Advanced Studies, Merrion Square North D02Y006, Dublin, Ireland. E-mail: maass@cp.dias.ie

Accepted 2025 February 17. Received 2025 February 14; in original form 2024 October 2

SUMMARY

Reflection imaging at volcanoes presents significant challenges due to the highly heterogeneous subsurface, which generates complex wavefields characterized by substantial wave scattering. These scattered waves obscure coherent energy, such as reflections from geological structures in the subsurface. In this study, we develop processing strategies to address the limitations of high-frequency (5–20 Hz) passive reflection imaging at Krafla, a volcanic caldera in NE Iceland. Krafla is among the few locations worldwide where magma has been encountered at 2.1 km depth when drilling the IDDP1 borehole. We analyse over 300 local microearthquakes and industrial noise recorded during five weeks in the summer of 2022. We show that wavefields lack coherency even between stations spaced at 30-m intervals due to the dominance of site effects beneath the stations. However, data coherency improves in the common-station domain, where different earthquakes recorded by a fixed station are analysed, thereby stabilizing the site effect. Spectral analyses in this domain reveal that site effects are partly due to resonances at the stations, likely caused by lava flows and cavities in the heterogeneous near-surface. By constructing a resonance removal filter, we successfully deconvolve resonance effects from the data, revealing previously masked coherent energy. We further reduce site effects by applying linear stacking of clustered earthquake traces and nonlinear amplitude weighting. Our approach significantly enhances coherency between stations and enables the identification of reflections in microearthquakes likely originating from the known magma-rock interface beneath the IDDP1 borehole.

Key words: Volcanic structure; Scattering; Spectral analysis; Seismic waves; Earthquakes; Magma.

1 INTRODUCTION

Seismic imaging of the Earth's crust is a widely utilized technique for visualizing and monitoring subsurface geological structures. At volcanoes, knowledge of magma chambers, fault systems and fluid pathways is essential for understanding their structure and dynamics, improving natural hazard assessment and optimizing geothermal energy exploitation. Numerous case studies have demonstrated the success of tomographic imaging in visualizing these features, using both earthquakes (e.g. Aloisi et al. 2002; Jaxybulatov et al. 2011; Pavez et al. 2019; Rezaeifar et al. 2024), and ambient seismic noise (e.g. Stankiewicz et al. 2010; Obermann et al. 2016; Urra-Tapia et al. 2023). However, seismic tomography integrates data from multiple seismic waves travelling along different ray paths between sources and receivers and thus depends highly on the ray coverage, defined by the distribution of sources and receivers at the surface. This averaging process often smooths out finer geological features, resulting in a broader, less detailed subsurface image.

In contrast, reflections of seismic waves depend on the gradient of seismic velocities. When the interface between two geological materials is sufficiently sharp in seismic impedance, an incident wave will reflect off that interface, producing a detectable signal in seismograms recorded on the Earth's surface (e.g. Yilmaz 2001). Reflections carry high-resolution information about the internal structure of volcanoes, including local faults, magma pockets and other details that may be blurred out by seismic tomography or attenuation studies. However, reflection imaging at volcanoes is particularly challenging due to the complexity of the wavefields, caused by extensive wave scattering within a highly heterogeneous subsurface. Both vertical and horizontal resolution depend on the wavelength (λ): as a rule of thumb, two reflectors at different depths should be separated by at least $\lambda/4$ to be distinguishable (e.g. Sheriff 1977; Okaya 1995). The Fresnel zone of a wave represents the area over which seismic wave energy is averaged horizontally. Its first radius is given by $\sqrt{\lambda z/2}$, where z is the depth of the reflector (e.g. Thore & Juliard 1999). Thus, high frequencies are needed to obtain a high-resolution image of the subsurface. However, the total scattering intensity increases with increasing frequency, as small wavelengths are more likely to interact with small-scale heterogeneities such as fractures and voids. These scattered waves can mask coherent reflections in the data, complicating data analyses and interpretation. Despite these challenges, the controlled-source seismic community has extensively explored and demonstrated the effectiveness of reflection imaging for achieving high-resolution images of the subsurface at volcanoes (e.g. Dello Iacono *et al.* 2009; De Barros *et al.* 2012; Matsumoto *et al.* 2012; Bruno *et al.* 2017; Barison *et al.* 2023).

Using passive sources (i.e. earthquakes and ambient seismic noise) is advantageous because it eliminates the need for costly and resource-intensive seismic wave generation, but also introduces additional challenges due to the often unknown, less predictable and more variable characteristics of the sources. Nonetheless, several studies demonstrate the potential of passive reflection imaging at volcanoes. For example, Thurber et al. (1989) analysed reflected phases in microearthquake seismograms and found evidence of a 0.8 km-thick low-velocity layer at 11.5 km depth beneath Mauna Loa volcano, Hawaii, which they interpreted as marine sediments. Matsumoto & Hasegawa (1996) used S wave reflections to delineate a thin (< 100 m) magma body between 8 and 15 km depth beneath Nikko-Shirane volcano, Japan. Byerly et al. (2010) identified several geological layers between 6 and 19 km beneath Montserrat by investigating reflections in microearthquakes recorded by 5 Hz geophones. Blondel et al. (2018) and Giraudat et al. (2024) applied seismic interferometry to retrieve Green's functions between geophones. They then constructed reflection matrices encapsulating the body wave propagation information contained in the retrieved transfer functions. Through various matrix operations and iterative time reversal, they unveiled the 3-D structure of Mt. Erebus volcano in Antarctica and La Soufrière volcano in Guadeloupe.

The work presented in this study focuses on Krafla, an active, 10 km-wide volcanic caldera in northeast Iceland (Fig. 1). The most recent eruptions, known as the 'Krafla fires', occurred between 1975 and 1984 along elongated fissures (e.g. Björnsson et al. 1977; Tryggvason 1994). Krafla is an important site for geothermal energy production in Iceland and has received worldwide attention as one of the few places where magma was encountered through drilling operations. In 2008, quenched silicic glass retrieved from well KJ-39 indicated the presence of magma at a depth of 2.6 km (e.g. Mortensen et al. 2010). Subsequently, in 2009, rhyolitic magma was unexpectedly encountered at the IDDP1 borehole at 2.1 km depth (e.g. Elders et al. 2011). Because of its importance for geothermal energy, it is an extensively studied volcano. However, despite multiple imaging studies (e.g. Einarsson 1978; Brandsdóttir & Menke 1992; Arnott & Foulger 1994; Brandsdóttir et al. 1997; Onacha et al. 2005), both magma pockets remained undetected before the drilling, but were addressed in several studies afterwards (e.g. Schuler et al. 2015; Kim et al. 2017). Kim et al. (2020) analysed reflections in microearthquake seismograms at Krafla and identified several reflectors around the IDDP1 borehole at the depth where magma was encountered.

During the summer of 2022, we conducted a 5-week long field campaign at Krafla, deploying more than 110 seismic stations in a reflection seismic configuration centred around the IDDP1 borehole. Our objective was to improve passive reflection imaging in complex media, using the known magma–rock interface beneath IDDP1 as a benchmark for our investigations. Here, we present a systematic investigation of limitations associated with shallow reflection imaging in complex settings and explore strategies to overcome them.

We first demonstrate that recorded wavefields at Krafla due to more than 300 local earthquakes are dominated by site effects, causing a lack of coherency even amongst stations spaced at 30-m intervals. We then show that site effects are partly due to seismic resonance effects underneath the stations and demonstrate their mitigation using a resonance removal filter. We further enhance the signal-to-noise ratio (SNR) of coherent phases through stacking and weighting techniques. Finally, we apply the established workflow to the area around the IDDP1 borehole. Our workflow considerably enhances coherency in the data and facilitates the detection of reflections likely originating from the magma-rock interface at 2.1 km beneath the IDDP1 borehole. The main goal of this work is to develop and refine methods for enhancing coherency in heavily scattered, incoherent seismic data, in order to enable the robust extraction of reflections from geological structures. Krafla serves as an optimal site for testing these methods, because the location of the magma pocket is precisely known through drilling.

2 DATA AND SEISMIC SOURCES

As part of the IMPROVE project, we deployed a network of 114 seismic stations during ~5 weeks between June 17th and July 26th in 2022 (Fig. 1). Our setup comprises 104 short-period (5 Hz) seismic nodes, spaced at 30 m intervals along two profiles. Profile L1 consists of 33 stations labelled from northwest to southeast as 'L1001, L1002,..., L1033' and spans approximately 1 km. Profile L2 comprises 71 stations labelled from north to south as 'L2001, L2002,..., L2071', covering roughly 2 km. Most stations only record the Z-component (1C), while 36 nodes in the northern areas of the profiles record three components (3C) of the ground motion. The sampling rate was 250 Hz. We also deployed ten 3C-short-period (1 Hz) seismometres as a circular array (ARR) with an aperture of 150 m, recording data at a sampling rate of 200 Hz. After a few days of recording, four stations were removed from the southern end of L2 and redeployed at selected locations outside the profiles and array. The maximum difference in elevation within the seismic network is 90 m. Iceland GeoSurvey (ÍSOR) kindly provided a seismic event catalogue for our recording period, along with 1-D velocity models for P and S waves in the Krafla region (Guðnason et al. 2023, and references therein). More than 300 local earthquakes occurred during our time period of analysis (Fig. 1b). Uncertainties for latitudes and longitudes are of the order of 0.5 km. Local magnitudes range between -0.47 and 1.45. Depths vary between 0.67 and 3.31 km b.s.l., with the majority occurring between 1 and 2 km. Depth uncertainties exceed 1 km for shallow events, but are generally of the order of 0.5 km. Throughout this work, instrument response-corrected data from the two profiles L1 and L2 will be shown.

3 LIMITATIONS OF REFLECTION SEISMIC IMAGING AT KRAFLA

Fig. 2 presents the earthquake with the largest local magnitude $(M=1.45\pm0.34)$ in the data set, recorded by all 33 stations of line L1. The event occurred at a depth of 1.78 ± 0.40 km b.s.l.. Vertical (Z) components, and, if available, radial (R) components (rotated towards the epicentre) are shown to provide an initial assessment of wavefields on both the vertical and one horizontal component. Time-series were filtered between 5 and 20 Hz using a second-order Butterworth band-pass filter. To enhance weak phases in the earthquake coda, an automatic gain control (AGC) (e.g. Dondurur

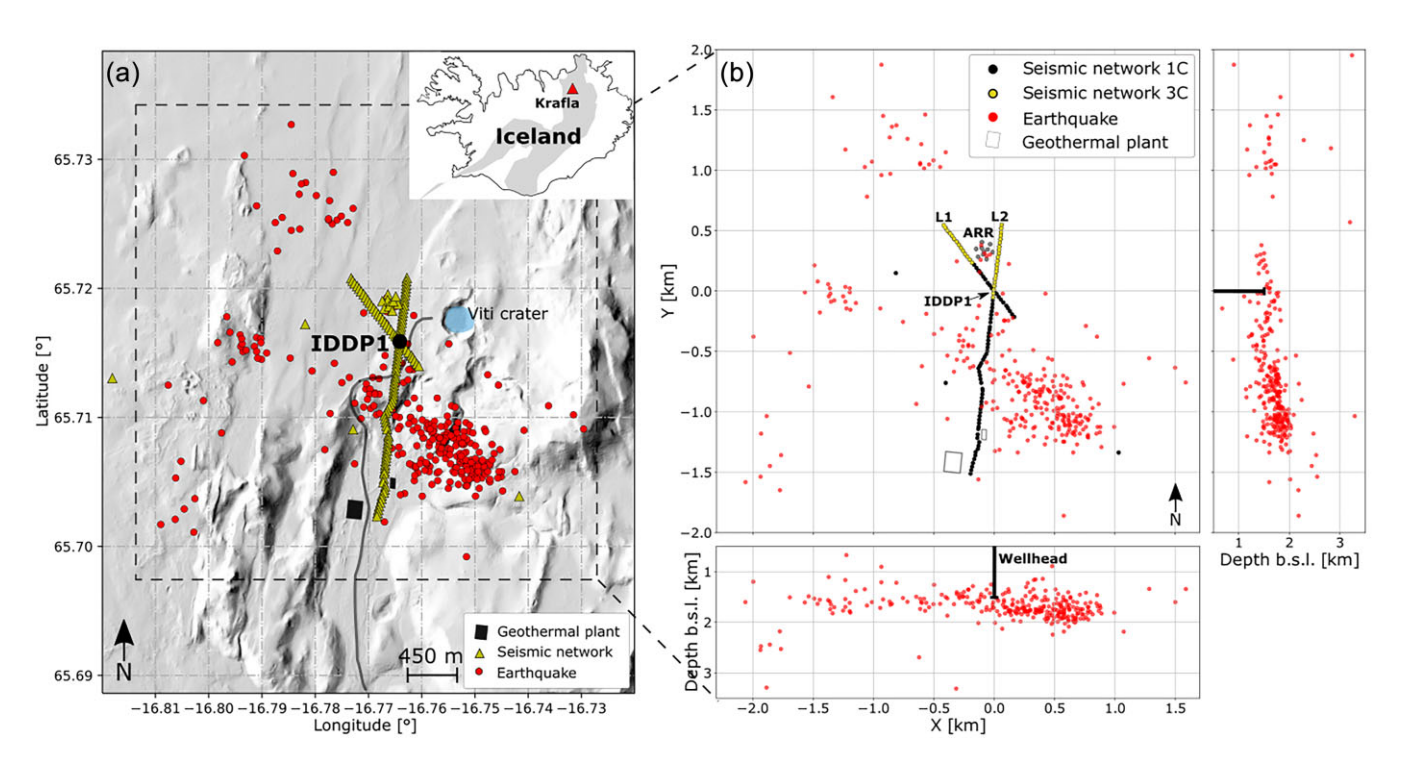


Figure 1. Study area. (a) Seismic network (yellow triangles) and earthquake locations (red dots) plotted onto a hillshade digital elevation model retrieved from https://atlas.lmi.is/mapview/?application=DEM. The grey thick line represents a road, and the black squares are the main buildings of the geothermal plant. The location of Krafla volcano in Iceland is indicated in the small map in the right corner of the image. (b) Detailed setup shown in the Cartesian coordinate system used in this study. The seismic network comprises two profiles (L1, L2) that intersect at the IDDP1 borehole and a circular array (ARR). The borehole trajectory at the IDDP1 where magma was encountered during drilling in 2009 is schematically indicated. Earthquake locations were determined and provided by ISOR (Iceland GeoSurvey).

2018) with a window length of 1 s was applied, and traces were normalized by their maximum absolute value. Theoretical arrival times for direct P- and S-waves were computed through ray tracing with the CREWES Matlab toolbox (Margrave 2000), based on 1-D velocity models (Fig. 2b). The Z- and R-components clearly show the onsets of direct P and S waves, demonstrating a reasonable match between theoretical arrival times and real data. Coherent phases can be observed in the P-wave coda. Following the S-wave arrival, both components record a scattered and incoherent wavefield. This occurs despite hypocentral distances being larger than 2 km, far exceeding the interstation distance of 30 m. Consequently, the ray paths of waves travelling from the hypocentres to the stations are nearly identical, differing significantly only in the final segment beneath the stations. The lack of coherency in the S-wave coda therefore indicates that waveforms are predominantly influenced by site effects within the near-surface beneath the stations. Analysis of the frequency content of the waveforms supports these observations. Fig. 2(d) shows power spectral densities (PSDs) of Z-component records for six neighbouring stations. The PSDs are derived from the filtered data without AGC applied and normalized relative to the maximum PSD value among all traces. PSDs vary in both magnitude and shape. All power spectra display distinct sharp peaks at specific frequencies. Four stations (L1013, L1014, L1015, L1016) feature single, dominant resonance peaks at different frequencies, while the other stations display multiple, more evenly distributed peaks. Thus, the earthquake produces a broad range of frequencies, but the energy distribution varies considerably across adjacent stations. These analyses suggest that site-specific conditions and structural features of various sizes underneath the stations trap and amplify different frequencies in the wavefields.

Another limitation arises from our station-earthquake configuration. Because of the limited extent of our study area (2 km x 1 km), the moveout of different phases across the profiles is similar. For example, in Fig. 2(c), both the *P* and *S* waves arrive at the stations with nearly identical apparent velocities. Coherency-based methods which aim to enhance the SNR of specific wave phases, typically rely on phases arriving with distinct apparent velocities to achieve constructive interference of the desired phase and destructive interference of others. However, in our scenario, because of the minimal differences in apparent velocities and the finite frequency content of waves, summation along a specific moveout does not result in destructive interference of other phases. This makes the application of commonly used coherency-based imaging methods challenging.

Overall, challenges of passive reflection imaging at Krafla are related to (i) the geological and physical properties of the subsurface and (ii) the geometry of our problem. While the latter arises from the specific station-earthquake configuration used in our study, the complexity of wavefields due to wave scattering and site effects is a common characteristic of geologically intricate environments (e.g. Martini & Bean 2002; O'Brien & Bean 2009; Bakulin *et al.* 2023). Reflections would be expected to appear as coherent energy in the coda of seismograms—the long wave trains following the direct waves (e.g. *P* and *S* waves). However, heterogeneous geological conditions and a dominance of site effects cause a severe lack of coherency in the coda, obscuring coherent energy reflected from layer boundaries of interest.

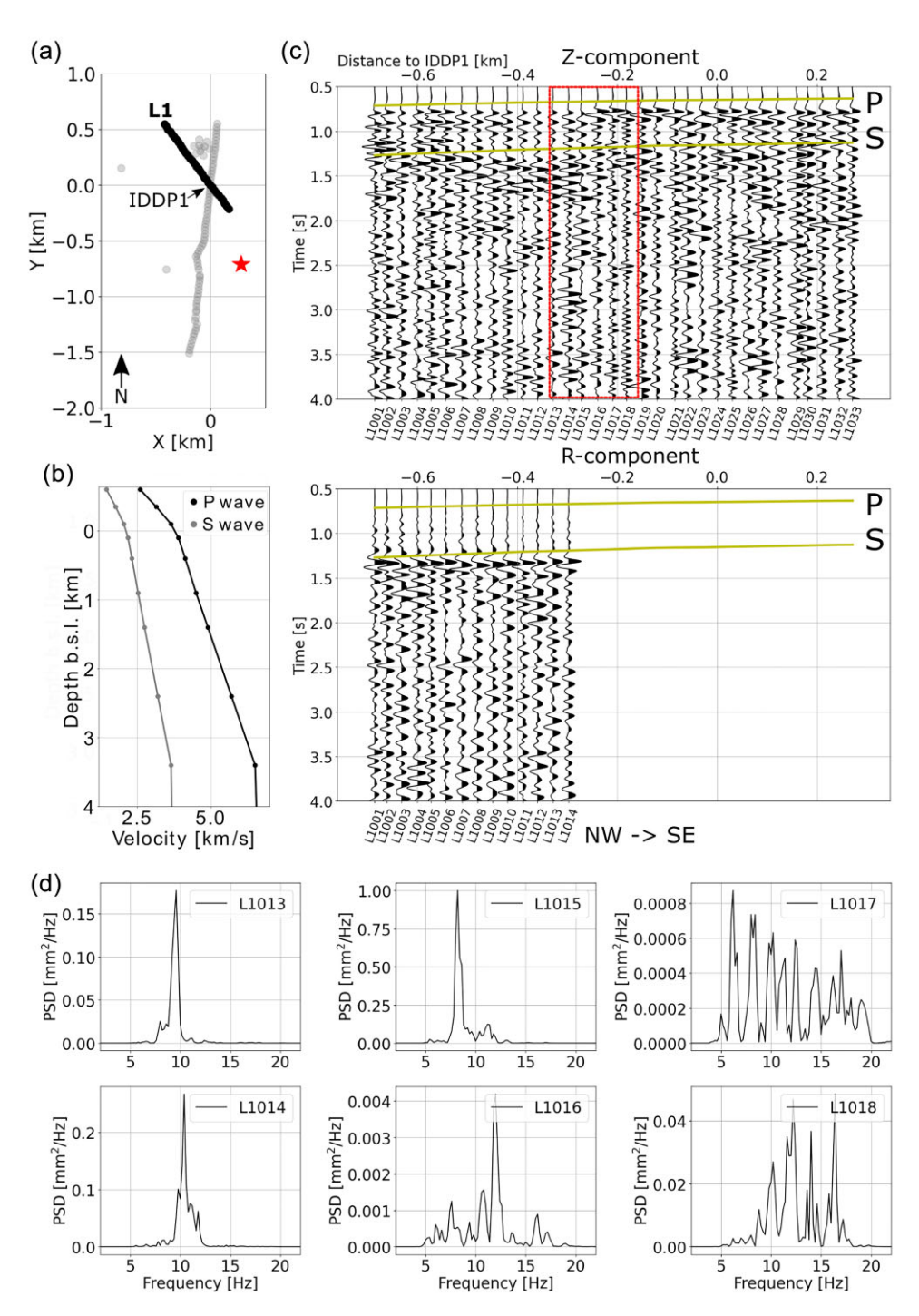


Figure 2. (a) Location of the earthquake (red star) shown in (c) and seismic stations (black dots). (b) 1-D velocity models provided by ÍSOR, used to compute theoretical arrival times for direct P and S waves. (c) Waveforms recorded by all stations along the approximately 1 km-long line L1 due to an earthquake on 2022-07-04 at 23:07:19 pm at a depth of 1.78 ± 0.40 km b.s.l., with a local magnitude of $M = 1.45 \pm 0.34$. The northernmost station is on the left, and the southernmost station is on the right. Vertical and, if available, radial components (rotated towards the epicentre), are shown. The x-axis displays station names. Theoretical arrival times for direct P and S waves (yellow lines) align well with onsets in the real data. (d) Power spectral densities (PSDs) as a function of frequency for the six neighbouring traces inside the red box in (c). Spectral characteristics vary considerably across the stations.

4 RESONANCE EFFECTS AS PART OF THE SITE RESPONSE

Certain earthquake traces show a distinct, pronounced resonance peak in their power spectra. In Fig. 2, one earthquake recorded by different stations is shown, in the following this is referred to as a 'common-earthquake-gather' (CEG). Data can also be analysed

in common-station-gathers (CSG), where different earthquakes are recorded by a fixed station. Fig. 3 shows an example of a CSG for station L1013 on profile L1, which displays > 50 events within an earthquake cluster in the south-east of our study area. These events were selected based on their spatial proximity and limited to a specific number for visualization purposes. Traces are sorted

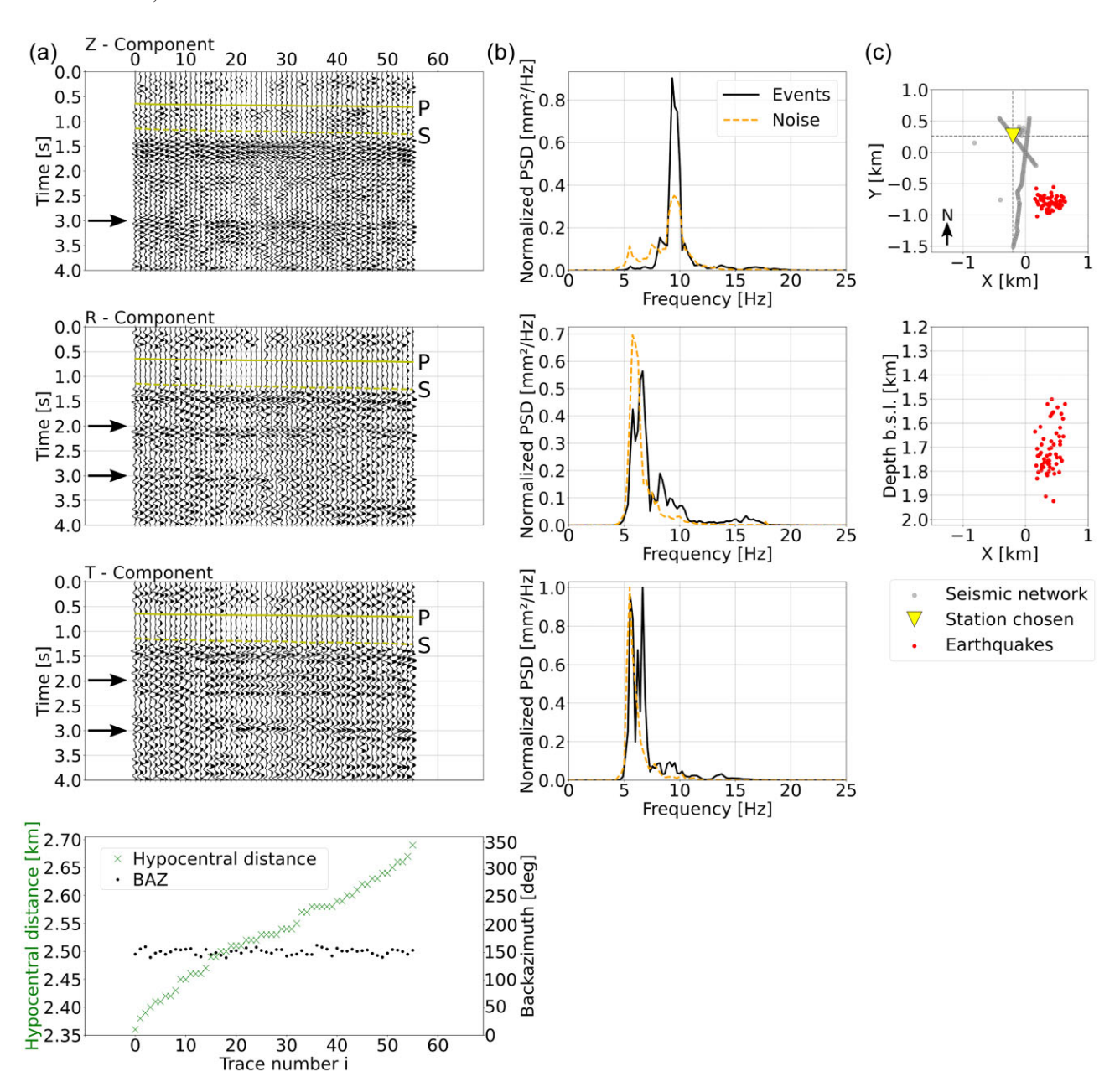


Figure 3. (a) Common-station gather (CSG), in which >50 events recorded by the fixed station L1013 are plotted next to each other. Vertical (Z), radial (R) and transverse (T) components are shown. Bandpass filtering (5–20 Hz) and automatic gain control with a window length of 0.8 s were applied to the data and traces are normalized by their peak amplitude. Selected earthquakes have similar backazimuths and traces are sorted according to their hypocentral distance, as illustrated in the bottom plot. The yellow lines are theoretical traveltimes of P and S waves, calculated using 1-D velocity models (see text). The arrows indicate times at which coherent arrivals are registered across multiple events. (b) Averages of power spectral densities (PSDs) computed for all traces shown in (a) (black lines) as well as for industrial noise from the geothermal plant (yellow lines). Standard deviations are not plotted for better visual comparison. Noise and earthquake traces show similar spectral curves. (c) Locations of the fixed station (yellow triangle) and locations of earthquakes included in the analysis (red dots).

by hypocentral distance to produce smooth moveout curves for direct waves and enhance the visibility of coherent phases. Data are filtered between 5 and 20 Hz with a second-order Butterworth bandpass filter. Automatic gain control with a 0.8 s window was applied to enhance the visibility of weak phases, and traces are normalized by their maximum absolute amplitude to compensate for amplitude differences between traces caused by factors such as event magnitudes. In comparison to the CEG, wavefields are more coherent and show distinct phases in addition to direct *P* and *S* waves, for example

at 3 s on all components. At 2 s, a coherent phase is registered on the radial component. It is unclear if this phase is also recorded on the Z-component. The presence of wave reverberations is evident. For example, shortly after the S-wave arrival, amplitudes increase on the Z-component, followed by reverberations at a distinct frequency with decreasing amplitude over time. A similar pattern is observed after 3 s. Overall, time-series exhibit a monochromatic character, with a single frequency dominating the wavefield (despite applying a broad-band filter between 5 and 20 Hz).

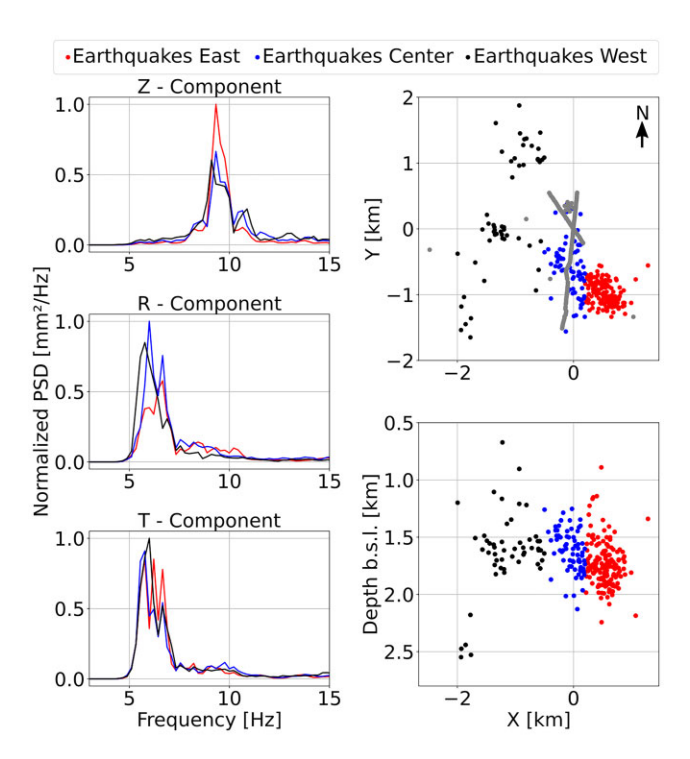


Figure 4. Power spectral densities (PSDs) of events from different geographical locations, calculated for the same station as in Fig. 3. The red, blue and black lines are averages of PSDs calculated for events in the east, centre and west of our study area, respectively. Similar frequency characteristics, resonance peaks and associated resonance frequencies are obtained independently of the backazimuth of the earthquakes. Standard deviations are not plotted for better visual comparison.

We calculate the averages of PSDs of all filtered earthquake traces included in Fig. 3(a) (without AGC applied) and for industrial noise from the geothermal power plant in the same frequency range, defined as 4 s-long time windows prior to each earthquake in the CSG. The results are shown in Fig. 3(b). Both noise and earthquake mean curves were normalized by the respective maximum PSD value across all components. The transverse component has the largest PSD values, followed by the radial and Z-components. A sharp resonance peak at 9.5 Hz on the Z-component and several nearby resonance peaks around 6 Hz on the horizontal components reflect the monochromatic character and reverberations in the time domain. Mean PSD curves for earthquakes and noise are similar, showing nearly identical resonance peak frequencies. This is despite the fact that noise is produced at the surface in the geothermal power plant (Fig. 1), whereas earthquake waves propagate from deeper sources, following different ray paths until converging beneath the stations. To ensure that the earthquake resonance peaks—and corresponding resonance frequencies are not unique to the selected earthquake cluster and to further exclude source effects, we repeat the analyses for other backazimuth ranges. Fig. 4 demonstrates that similar, nearly identical resonance peaks (and resonance frequencies) are obtained regardless of the geographical location of the events. Hence, in contrast to the CEG in Fig. 2, where adjacent stations only 30 m apart displayed significantly different frequency responses for the same earthquake, the frequency responses of a fixed station for different earthquakes spread over an area larger than 3 km x 3 km are nearly identical.

Resonance peak frequencies are independent of the source mechanism and geographical location. These observations confirm that

resonance effects predominantly arise in the shallow subsurface layers directly beneath each station due to the local structure interacting with the incoming wavefield, resonating at specific frequencies. Cuttings from the IDDP1 well show that the uppermost ~ 1.4 km of the subsurface consists of alternating layers of basaltic lava and hyaloclastites (Mortensen et al. 2014), which are a heterogeneous mixture of different rock types like breccias and tuffs. Therefore, the observed resonances and scattering are likely due to combinations of loose volcanic rocks, cavities and subsurface layering with significant impedance contrasts. These geological features, varying in size and extent, result in different resonance frequencies across stations and station components, contributing to site effects and the lack of coherency in common-earthquake gathers (Fig. 2). In the common-station domain, however, fixing the station 'stabilizes' the site effect, allowing for coherent arrivals to be observed across multiple events recorded at the same station.

5 REDUCTION OF SITE EFFECTS IN THE DATA

We investigate whether site effects can be reduced to reveal potentially coherent energy in the underlying wavefields. First, we introduce a resonance removal filter to reduce the influence of wave reverberations discussed in the previous section. This is followed by linear stacking of earthquake traces and nonlinear amplitude weighting. Here, we exemplify the processing with the Z-component records of station L1013 (Fig. 3a and Fig. 6).

5.1 Resonance removal filter

A seismogram A(t) recorded on the surface can be modelled as the convolution of the source time function s(t), the Green's function G(t) that describes wave propagation from source to receiver, and the instrument response r(t), with added incoherent (e.g. instrumental or ambient) noise n(t). This is mathematically expressed as $A(t) = s(t) \star G(t) \star r(t) + n(t)$ where \star denotes convolution. The propagation term can be split up into the main propagation component $G_m(t)$, which accounts for the propagation of seismic waves in the medium between the source and the site, and a site-specific term $G_s(t)$, which represents the transfer function describing wave propagation through the medium immediately beneath the station. In this scenario, and after deconvolution of the instrumental response (which is typically known), the convolutional model can be written as

$$A'(t) = s(t) \star G_m(t) \star G_s(t) + n'(t), \tag{1}$$

with $A'(t) = A(t) \star r^{-1}(t)$ and $n'(t) = n(t) \star r^{-1}(t)$. Because site effects dominate the wavefields at Krafla, $G_s(t)$ is the governing term in eq. (1). The coherency in the common-station domain suggests that the information contained in common-station gathers can be used to address resonance effects and, consequently, part of the site term $G_s(t)$ in eq. (1). The goal is to subsequently deconvolve $G_s(t)$ from eq. (1) to isolate the primary propagation term $G_m(t)$, which encompasses the Earth's main propagation effects, including refractions and reflections from deeper geological structures of interest.

A commonly used method to reduce the influence of monochromatic signals is spectral whitening (e.g. Bensen *et al.* 2007; Weemstra *et al.* 2014; Tauzin *et al.* 2019; Fichtner *et al.* 2020). This technique smooths the amplitude spectrum either by equalizing spectral amplitudes or by applying a running mean average over a set number

of points. However, spectral whitening alters amplitudes across the entire frequency range of a signal, leading to a loss of true amplitude information. In marine seismology and receiver function analyses, resonance removal filters have been used to mitigate reverberations within sedimentary layers and water columns (e.g. Backus 1959; Akuhara & Mochizuki 2015; Yu et al. 2015; Cunningham & Lekic 2019; Zhang & Olugboji 2021, 2023). These filters have the form of a complex exponential function in the frequency domain

$$F_{\text{CE}}(f) = 1 + A \exp(-2\pi i f t_0),$$
 (2)

where f is frequency, A represents the reverberation strength and to is the two-way traveltime of the reverberation. This approach assumes that reverberations can be modelled by waves trapped within a low-velocity waveguide, repeatedly reflecting between the surface and its lower boundary due to strong impedance contrasts and an amplitude decay depending on the reflection coefficients (e.g. Backus 1959). In the frequency domain, these reverberations manifest as sharp peaks at the fundamental resonance frequency and its overtones (e.g. Zhang & Olugboji 2021). The filter represented by eq. (2) essentially acts as the inverse of the reverberation response with notches at the resonant frequencies and an amplitude scaled by the strength of the reverberation, effectively suppressing the reverberations and mitigating their impact on the seismic signal. For a detailed derivation of eq. (2), we refer the reader to Backus (1959), Yu et al. (2015) and Zhang & Olugboji (2021). We evaluate the effectiveness of this filter for reducing site effects in our data. In addition, we test a filter design based on a Gaussian function $F_G(f) = 1 - A \exp\left(\frac{-(f - f_0)^2}{2\sigma^2}\right)$, where f_0 is the resonance frequency and σ the standard deviation of the Gaussian distribution. For easier parametrization, we replace σ and express the Gaussian function in terms of its full-width at half maximum $w = 2\sigma \sqrt{2 \ln(2)}$, yielding

$$F_G(f) = 1 - A \exp\left(\frac{-4\ln(2)(f - f_0)^2}{w^2}\right). \tag{3}$$

The required parameters for the filters are determined by means of autocorrelation. At first, autocorrelations of all traces included in the CSG from Fig. 3(a) and their amplitude spectra are calculated. To increase the robustness of the analysis, we smooth the mean spectral curve using Konno-Ohmachi smoothing (Konno & Ohmachi 1998) with a bandwidth of 60 points. Smoothing is particularly recommended in cases where limited data are available and data quality is poor, for example, when monochromatic noise sources generate spikes in the amplitude spectrum with amplitudes exceeding those of the resonance peak. Additionally, smoothing is beneficial when multiple closely spaced resonance peaks with comparable amplitudes are present, such as those observed on the horizontal components in Fig. 3(b). In such cases, smoothing effectively averages over the peaks, preventing the algorithm from targeting only the peak with the higher spectral amplitude and failing to detect and properly deconvolve the other one. Alternatively, and generally if multiple resonance frequencies are present, the algorithm can be applied iteratively to isolate and process individual spectral peaks sequentially.

The resonance frequency (f_0) is identified as the frequency with the peak spectral amplitude in the smoothed mean spectral curve, and the width of the spectral peak (w) corresponds to the distance between the frequencies at which the function reaches half of the peak amplitude. Figs 5(a) and (b) demonstrate that the autocorrelation process smooths out frequencies higher and lower than the

resonance frequency. Fig. 5(c) illustrates that the stack of autocorrelations in the time domain exhibits multiple minima and resembles a decaying sinusoid. By fitting a decaying sine curve to the stack, A and t_0 can be determined as the absolute amplitude of the first minimum in the sine curve and the corresponding lag time (Cunningham & Lekic 2019). Note that the fitted decaying sinusoid can be interpreted as the average site response accounting for seismic resonance effects at the station, and thus as part of the transfer function $G_s(t)$ in eq. (1). Crucially, all parameters needed for the design of the filters can be determined without relying on *a priori* knowledge of the elastic properties of the reverberant structures.

Using these parameters, the filters are designed according to eqs (2) and (3) (Fig. 5d). Both the complex exponential (F_{CE}) and Gaussian (F_G) filters exhibit a local minimum at the resonance peak frequency. Unlike the complex exponential filter, the Gaussian filter maintains a flat amplitude response on either side of the resonance frequency. We multiply the original complex spectrum of each trace from the CSG (Fig. 3a) with the designed filters to deconvolve the resonance peak from the data. The outcomes for an example trace are shown in Figs 5(e) and (f). Both filters are effective in reducing the resonance peak and preserving the general shape of the amplitude spectrum. The choice between the Gaussian filter and the complex exponential filter depends on the data characteristics and the specific objectives of the study. The Gaussian filter has a narrower pulse width, and its application leaves the frequency content largely unchanged except at the resonance frequency and its direct vicinity. In contrast, the complex exponential filter, with its broader pulses and periodic nature, also amplifies frequencies both above and below f_0 , leading to more significant modifications of the true amplitudes. However, it is advantageous in its ability to account not only for the fundamental mode but also the overtones of the reverberations and may therefore be more appropriate in cases where higher frequency resonance components are prominent in the data. In this study, however, we focus on stations where a single, dominant resonance peak is observed. Overtones, which occur at odd multiples of the fundamental frequency, are either strongly attenuated, obscured by other earthquake signal components at higher frequencies or lie outside the analysed frequency range. For instance, on the horizontal components in Fig. 3, where the fundamental resonance frequency is approximately 6 Hz, no significant spectral amplitude increase is observed at the expected overtone frequency of 18 Hz. On the vertical (Z) components, the overtone at 28.5 Hz falls outside the analysed frequency range (5–20 Hz). Therefore, to ensure the least distortion of true amplitudes within the analysed frequency range, we choose the Gaussian filter for further analyses.

The filtered spectra are now transformed back into the time domain using the inverse Fourier transform. The result is shown in Fig. 6(b). The deconvolution successfully reduces reverberations in the CSG, for example after the arrival of the direct *S* wave and after the coherent phase at 3 s. The arrival at 2 s on the radial component, whose presence on the *Z*-component was previously speculative (Section 4), is now clearly discernible. Another arrival, previously masked by reverberations, can be detected at about 3.5 s.

5.2 Linear stacking and nonlinear amplitude weighting

In order to further reduce site effects and incoherent scattering, we employ two additional processing steps which exploit the lateral coherency of traces in the CSG. At first, we apply linear stacking to the data. This is achieved by using a running-mean average, where each trace in the CSG is redefined as the mean of a number of

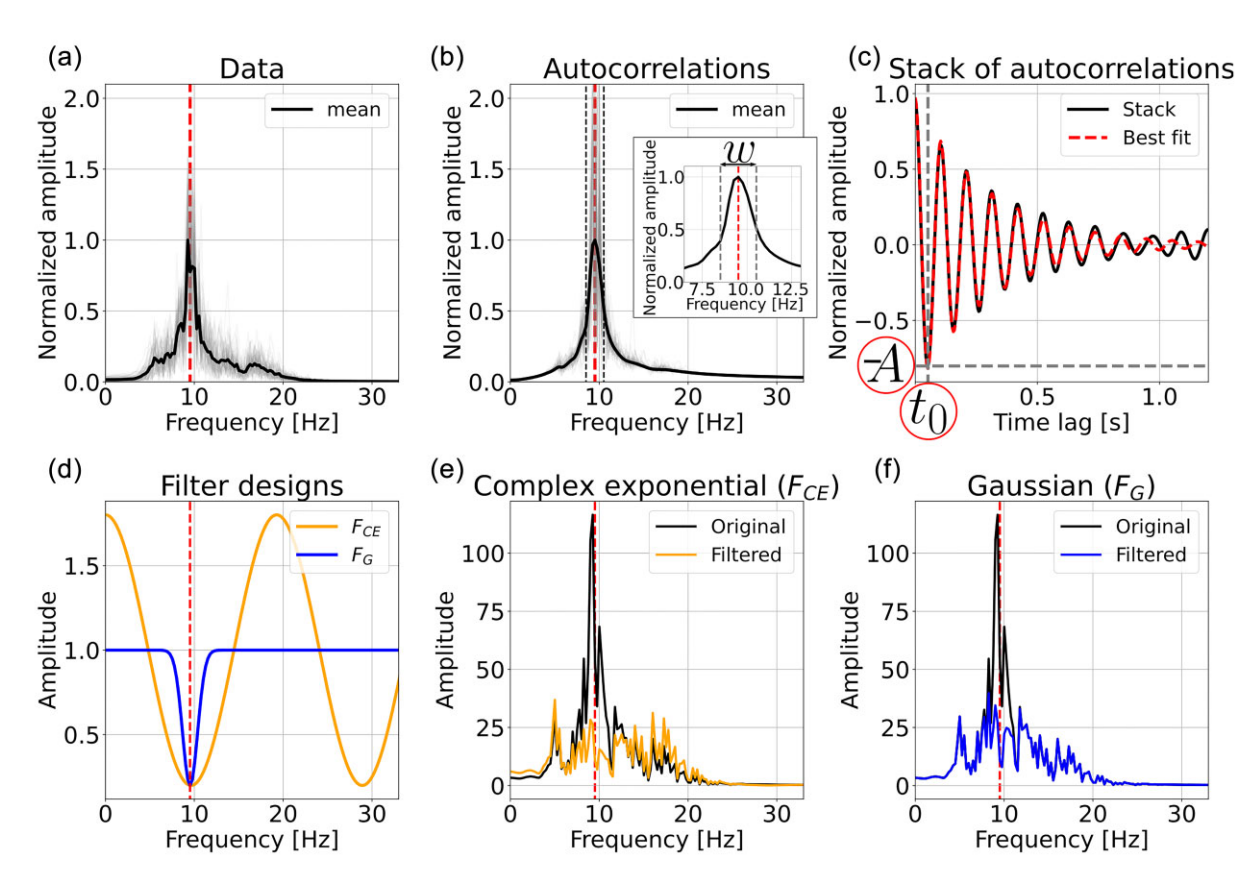


Figure 5. Procedure for constructing the resonance removal filters. (a) Amplitude spectra of all traces from the CSG (Fig. 3a) and their mean. (b) Amplitude spectra of all autocorrelations of traces and their mean after applying Konno-Ohmachi smoothing (see text). The small inset provides a more detailed view of the resonance peak. The red dashed line marks the resonance frequency $f_0 = 9.5$ Hz. The grey dashed lines indicate the full-width at half maximum (w) used in designing the Gaussian filter (F_G). (c) Positive lag times of the mean of all autocorrelations in the time domain (black line) resembling a fitted decaying sine curve (red line). The reverberation strength A corresponds to the absolute amplitude of the first minimum in the sine fit, and its corresponding lag time t_0 is the two-way traveltime of the reverberation. (d) Filter designs in the frequency domain. Both the complex exponential filter F_{CE} and the Gaussian filter F_G exhibit a minimum at the resonance frequency. (e–f) Comparison between the original and filtered amplitude spectra of an arbitrary event from Fig. 3(a). The resonance peak is clearly reduced in the filtered data.

neighbouring traces

$$a_i'(t) = \frac{1}{N_s + 1} \sum_{i=i-N_s/2}^{i+N_s/2} a_j(t), \tag{4}$$

where a_i is the amplitude of trace number i in the CSG at time t and N_s+1 the number of stacked traces. To further enhance the SNR of coherent phases, amplitudes are weighted in a nonlinear fashion: for a given trace $a_i'(t)$, the previous processing step (linear stacking) is repeated to obtain a stack over a pre-defined number of traces $a_i''(t) = \frac{1}{N_w+1} \sum_{j=i-N_w/2}^{i+N_w/2} a_j'(t)$. Then, the envelope of the stack is calculated $e_i''(t) = \sqrt{a_i''(t)^2 + \tilde{a}_i''(t)^2}$, where $\tilde{a}_i''(t)$ denotes the Hilbert transform (e.g. Liu 2012) of $a_i''(t)$. This envelope is multiplied with $a_i'(t)$

$$a_i'''(t) = a_i'(t)e_i''(t)$$

= $a_i'(t)\sqrt{a_i''(t)^2 + \tilde{a}_i''(t)^2}$. (5)

The selection of parameters N_s and N_w depends on the data quality and the objective of the study. Higher values of N_s and N_w enhance coherent phases across multiple earthquakes in the CSG, revealing the structure seen on average by the events, but smooth out fine details contained in individual earthquakes. At the edges of the CSG, the calculation of the means according to eq. (4) is adjusted to account for the limited number of traces available.

Specifically, when the centre trace i lacks sufficient neighbouring traces on one side, the stack is computed using the available traces. For example, if $N_s=2$, the leftmost (or rightmost) trace in the CSG would be calculated using itself and the adjacent trace to its right (or left). Due to the reduced trace count at the edges, the overall SNR and coherence of phases may be lower for events at these positions compared to those in the centre of the common-station gather.

Figs 6(c) and (d) illustrate the effect of linear stacking and nonlinear amplitude weighting with $N_s = 2$ and $N_w = 4$ on the data. Coherent phases stand out more clearly in the processed CSG and the overall SNR is improved. Both linear stacking and nonlinear amplitude weighting suppress incoherent scattering and noise (represented by n'(t) in eq. (1)). Note that our approach assumes an infinite apparent velocity across the traces included in the stacks. In our setting, due to the spatial proximity of events within the selected earthquake cluster and the sorting by hypocentral distance, we found that traveltime differences between phases in adjacent traces were negligible, justifying this assumption and eliminating the need for trace alignment before stacking. However, if significant traveltime differences are observed, alignment techniques (e.g. cross-correlation) should be applied before stacking to ensure constructive interference of coherent phases during the stacking process.

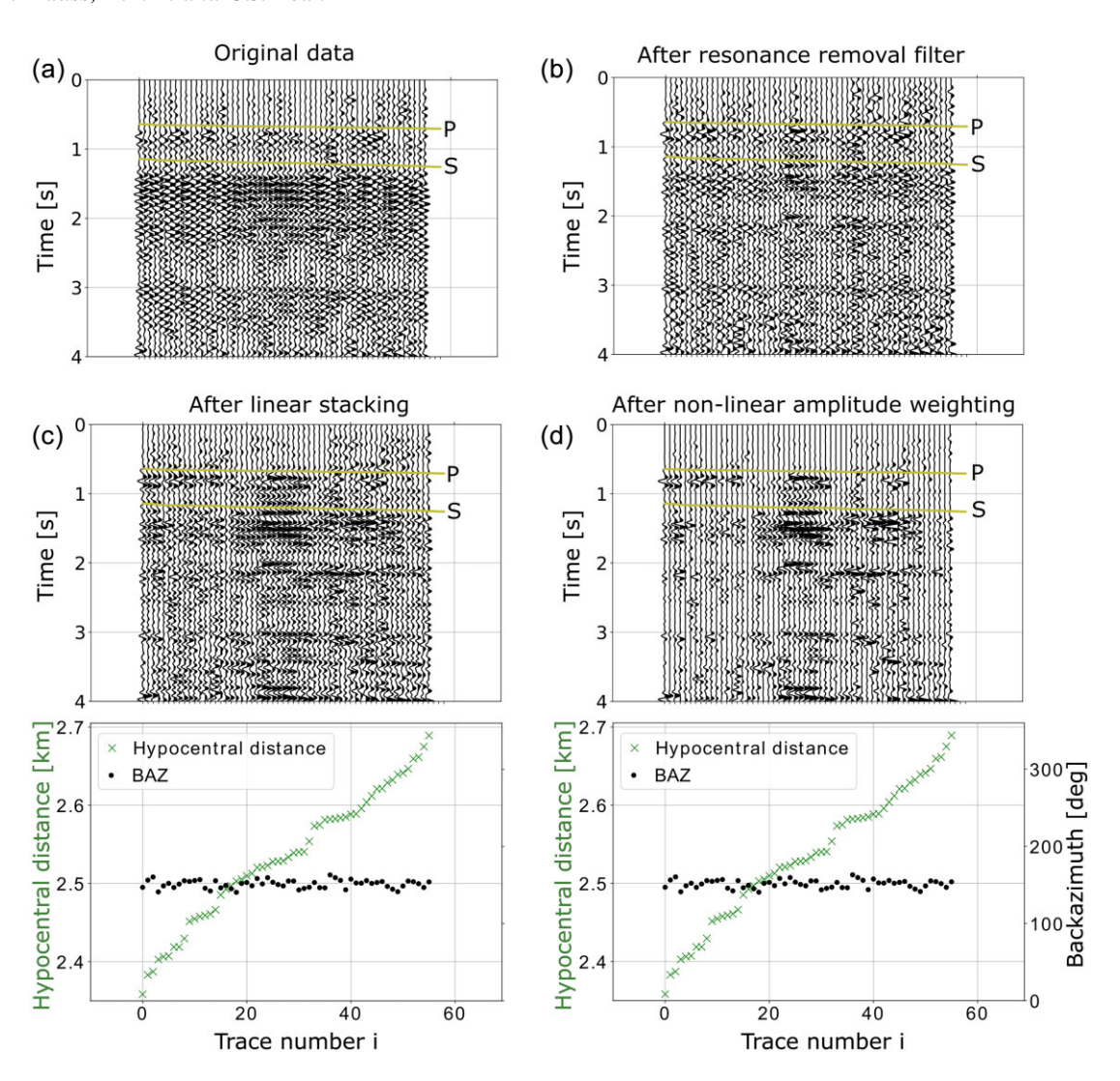


Figure 6. Processing scheme for enhancing coherent arrivals in common-stations gathers. The CSG for station L1013 is shown (same as in Fig. 3a). Data are sorted according to the hypocentral distance and earthquakes have similar backazimuths (BAZ), as shown in the bottom plots. (a) Original data. (b–d) Data after application of the resonance removal filter, linear stacking according to eq. (4) and nonlinear amplitude weighting according to Section 5 (see text).

6 EARTHQUAKE REFLECTION IMAGING AT THE IDDP1 BOREHOLE

We now demonstrate that the developed processing strategies enhance coherency between the stations and facilitate passive reflection imaging at Krafla. Our goal is to extract reflections from the recorded wavefields to image the subsurface around the IDDP1 borehole, using the known magma-rock interface encountered in 2009 at a depth of 2.1 km (1.5 km b.s.l.) as a reference point. We examine seventeen earthquakes close to the IDDP1 borehole, recorded by all twenty-one 3C-stations from profile L2 (Fig. 7a). These events are chosen because their proximity to each other and to the IDDP1 borehole ensures that seismic waves sample similar subsurface structures and predominantly provide insights into the area around IDDP1. Moreover, by reducing the distance the seismic waves travel from the hypocentres to the target area, we minimize scattering and distortions that occur as the waves propagate through the volcano. Stations near the borehole on line L1 lack three-component recordings (Fig. 1), and are therefore excluded from this analysis. Event depths range from 1.35 to 1.66 km b.s.l. with uncertainties between 0.4 and 0.7 km, placing them either just below or slightly above the magma–rock interface at 1.5 km depth. However, the substantial depth uncertainties suggest that all events could potentially occur above the interface. In addition, variations in the velocity model could influence the event locations. For instance, slightly lower seismic velocities than those assumed in the local velocity model would shift events that occur below the interface to positions just above it.

Primary reflections—waves travelling directly from the source to the interface and then to the stations—are only generated by events located above the interface. However, isolating these reflections in our data set is challenging. For events near the interface, primary reflections would arrive almost simultaneously with the direct waves, complicating their separation in the wavefields. For shallower events, the reflection may be indistinguishable from near-surface reverberations. Thus, even though primary reflections are generally preferred for reflection imaging due to their shorter ray paths, their presence in the wavefields is uncertain and their isolation challenging. For these reasons, we focus on multiple reflections, which arrive later in the seismograms. In particular, we investigate 'ghost reflections'—waves travelling from the hypocentre to the

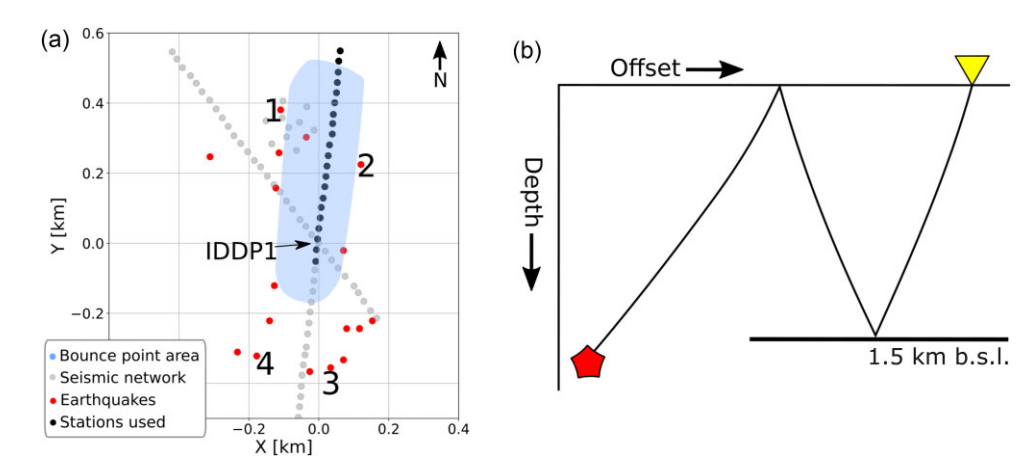


Figure 7. Setup for imaging the area at the IDDP1. (a) The selected twenty-one 3C-stations on profile L2 (black dots) and seventeen earthquakes (red dots) are shown. Results for the four indicated events are shown in Fig. 8. The area covered by bounce points of ghost reflections from an interface at 2.1 km depth is marked in blue. (b) Schematic ray path of ghost reflections bouncing off at a flat interface at 1.5 km b.s.l. (2.1 km below the surface).

surface, down to the interface, and up to the station (Fig. 7b). This wave type is generated independently of the source location. We compute expected arrival times of direct phases and ghost reflections using 1-D velocity models and the ray tracer introduced in Section 3 by assuming a flat interface at 1.5 km depth b.s.l.. We consider various phase combinations: pure *P* and *S* wave ghost reflections (P-P-P and S-S-S), as well as P-to-S converted phases (P-P-S and P-S-S). We also calculate X and Y coordinates of bounce points at 1.5 km depth b.s.l.. Fig. 7(a) shows that the bounce points computed for all considered ghost reflections fall within the blueshaded area and are thus located within and north of the IDDP1 borehole area.

The processing of data is carried out in the common-station domain for each station individually. At first, we create CSGs for every station, with each gather containing the seventeen selected earthquakes. The traces are sorted by their hypocentral distances to minimize traveltime differences between coherent phases on adjacent traces within the CSGs. We apply a zero-phase Butterworth bandpass filter between 5 and 20 Hz. Frequencies below 5 Hz are excluded due to interference of noise from the geothermal plant, while frequencies above 20 Hz resulted in image degradation from high levels of scattering. We remove the mean and linear trends from the time-series. Then, we apply the Gaussian resonance removal filter (Section 5.1) to each CSG to mitigate wave reverberations beneath the stations. Following this, we apply linear stacking and nonlinear amplitude weighting with parameters $N_s = 4$ and $N_w = 4$ to boost the SNR of coherent phases in the CSGs. These values were chosen after testing various parameters, as they improve the SNR of coherent phases across multiple events while preserving details from individual earthquakes. After applying the processing steps to all twenty-one CSGs, the traces are reorganized into commonearthquake gathers (CEGs). Fig. 8 compares the radial components of the processed CEGs for four events, whose epicentres are shown in Fig. 7(a), to the original data. The original data were only bandpass filtered between 5 and 20 Hz and detrended, with no further processing applied. An automatic gain control (AGC) with a window length of 1 s was then used in both the original and processed CEGs to improve the visibility of weak phases in the earthquake codas.

In the original data, extended monochromatic wave trains dominate the wavefields. These reverberations were discussed in detail in previous sections. While some consistent arrivals are visible,

such as in the northernmost part of the profile (stations L2001 to L2004), the data lack clear, distinct phases that can be isolated from the rest of the time-series, impairing the reliable identification of phases for subsurface imaging. While the processed data remain complex, the impact of monochromatic wave reverberations is significantly reduced. A distinct phase emerges near 2.5 s, most clearly visible in events three and four. To get an estimate of the average signals recorded by all stations, we compute the mean of all (twentyone) time-series contained in each processed (but not gained) CEG, resulting in a total number of seventeen stacks. These stacks are presented in Fig. 9 for all components. AGC with a window length of 0.8 s was applied to the stacks and traces are normalized by their respective maximum absolute amplitude. Theoretical traveltimes for direct P and S waves as well as for ghost reflections are indicated with arrows. We present two versions of the figure: one without the traveltime curves of modelled waves to avoid visual bias, and one with the traveltime curves to compare the theoretical moveouts with the real data.

The stacks highlight the coherency of the processed wavefields, with several distinct arrivals visible on each component. The arrival around 2.5 s on radial components is pronounced in all stacks of radial components. Its moveout aligns closely with the theoretical traveltime curve for a P-S-S ghost reflection. Another arrival at approximately 2 s matches the predicted traveltime curve for a P-P-S ghost reflection. At about 2.75 s, at the expected arrival time for an S-S-S ghost reflection, a coherent phase is also visible on the radial components, although its moveout does not match the modelled curve as precisely as the earlier arrivals. On the Z-components, several phases are evident within the P- and S-wave codas, including a coherent phase arriving at the predicted traveltime for a P-P-P ghost reflection. Another coherent phase appears shortly after 2 s, arriving slightly later than the potential P-P-S ghost reflection observed on the radial components. Its similar moveout suggests it may correspond to a near-surface conversion of the P-P-S ghost reflection. Coherency is also observed on the transverse components, with the most prominent phase arriving at approximately 2.2 s. To summarize, multiple distinct and coherent phases are observed across all components, likely representing refractions and reflections from subsurface geological structures. Notably, several arrivals align well with theoretical traveltime predictions for P-P-P, P-P-S, P-S-S and S-S-S ghost reflections, modelled for a flat interface at a depth of 2.1 km below the surface (or 1.5 km b.s.l.). These arrivals are

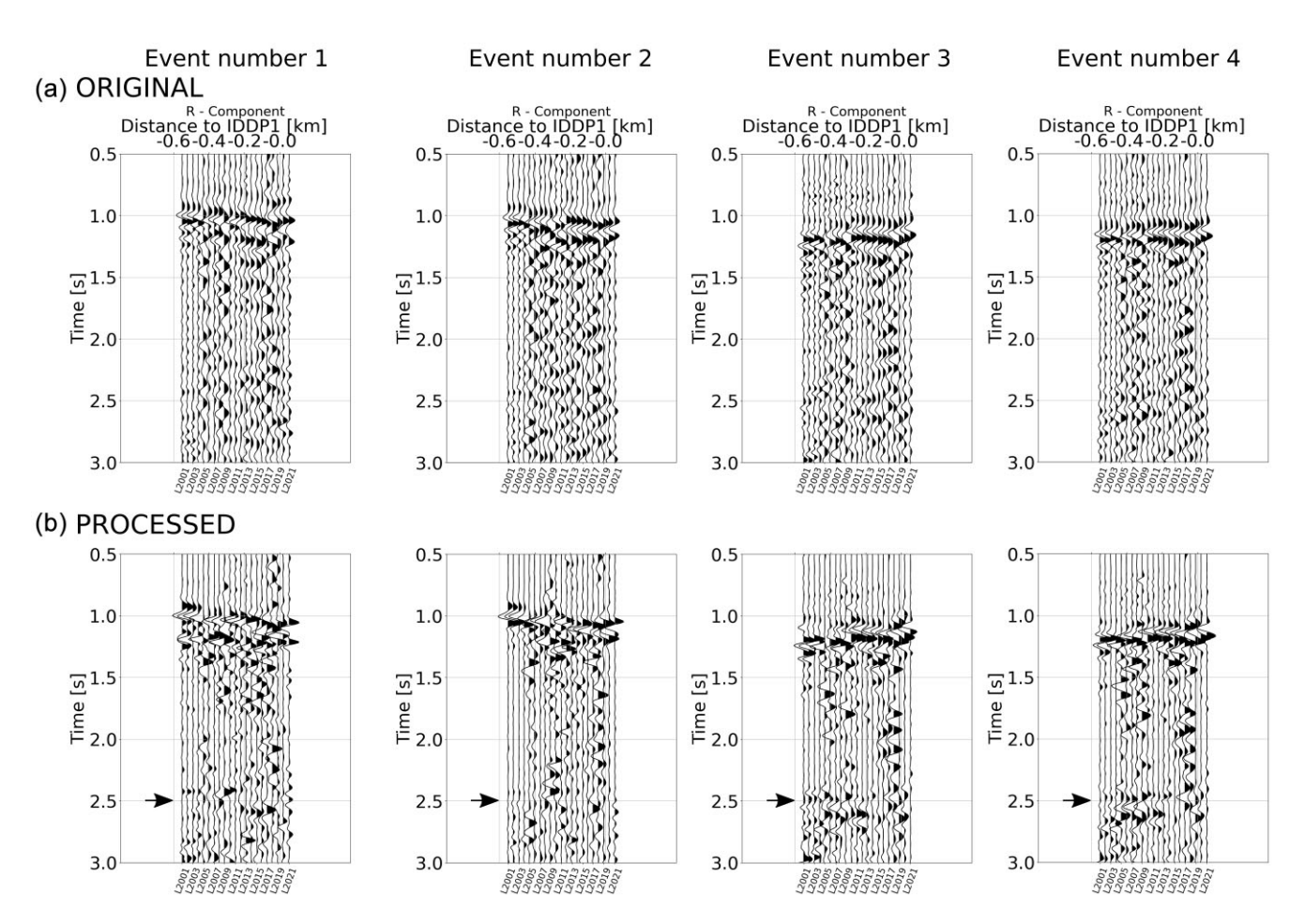


Figure 8. (a) Original and (b) processed CEGs (radial components) for four selected events whose epicentres are indicated in Fig. 7(a). A bandpass filter retaining frequencies between 5 and 20 Hz and AGC with a window length of 1 s was applied to both original and processed data (see text). The processed data show reduced reverberations and an arrival at 2.5 s.

therefore consistent with expected reflections from the known magma pocket beneath the IDDP1 borehole. In Section 7.3, we will further discuss and interpret our findings.

7 DISCUSSION

7.1 Common-station versus common-earthquake domain

In Section 3, we demonstrated that data lack coherency even between adjacent stations separated by 30 m. However, as shown in Section 4, data were more coherent in the common-station domain. By analysing multiple earthquakes recorded by the same station, we stabilized the site effect, resulting in more coherent wavefield characteristics compared to the more commonly analysed commonearthquake domain. We also found that similar resonance peak frequencies were obtained regardless of the backazimuth of the events (Fig. 4). Thus, in the case of the strong resonance observed here, applying the resonance removal filter does not require seismicity to be organized in clusters. Instead, it can be diffuse, with individual events occurring at different backazimuths. When clusters of seismicity are available, allowing waves to sample similar subsurface structures, stacking and weighting techniques in the commonstation domain can be applied to enhance the average response due to structure, thereby reducing incoherent scattering in the data (Section 5.2). Our analyses highlight the benefits of studying seismic data in the common-station domain. We therefore suggest the analyses of seismic data in the common-station domain at volcanoes and in complex geological settings where site effects strongly influence the wavefields. Especially when clusters of seismicity are available, the common-station domain offers multiple options for enhancing the SNR of coherent phases. However, even if seismicity is more diffuse, the common-station domain helps to reduce the impact of site effects in the data, revealing previously masked phases.

7.2 Distortion of true amplitudes and preservation of polarities

Amplitudes and polarities of reflections are important wavefield attributes which provide information about subsurface conditions at the reflector. High amplitudes are caused by large impedance contrasts, indicating sharp lithological changes. Polarities of reflections depend on the sign of the reflection coefficient. A change in polarity is expected for P and SV waves if the layer below the reflector has lower impedance than the upper layer. Thus, both amplitudes and polarities carry crucial information about rock types, density, porosity and fluid saturation at the interface. At volcanoes, interpreting amplitudes and polarities can be challenging. High levels of intrinsic and scattering attenuation lead to significant energy loss, necessitating artificially boosting amplitudes. Also, the heavily scattered, complex wavefields often obscure phase onsets, hindering the

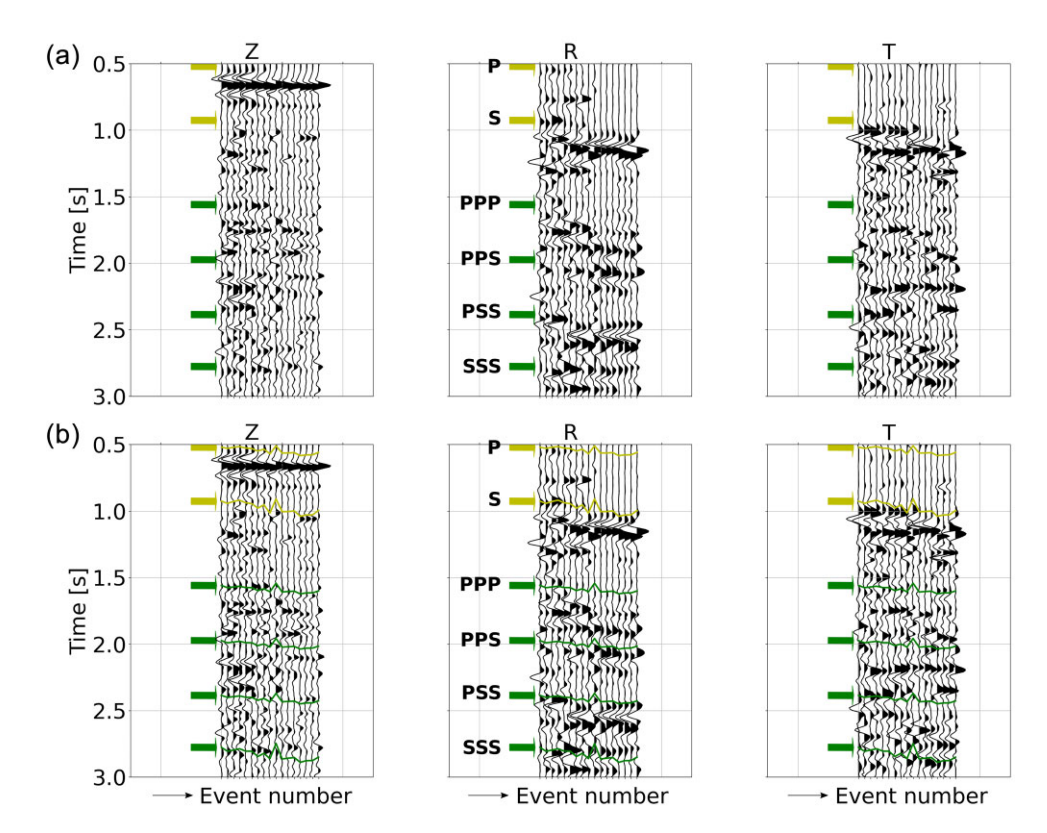


Figure 9. The seventeen stacks of all twenty-one time-series from each processed CEG (vertical, radial and transverse components), representing the average signal produced by the respective earthquakes. AGC with a window length of 0.8 s was applied to enhance the visibility of weak phases in the wavefields. Yellow arrows and lines mark expected arrival times of direct *P* and *S* waves, and green arrows indicate expected arrival times for different types of ghost reflections (see text). Two versions of the same plot are provided in (a) and (b), one without and one with traveltime curves.

reliable interpretation of polarities. In this work, we applied linear stacking and nonlinear amplitude weighting. These techniques boost the SNR of coherent phases but average out amplitude variations, leading to a loss of detailed amplitude information. Additionally, we employed AGC, which normalizes amplitudes within a moving time window to enhance weak phases in the seismograms. While AGC improves the visibility of these weak phases, it distorts true amplitudes. Consequently, several processing steps were applied that prevent the direct interpretation of amplitudes of reflections in our data. In contrast, our workflow preserves polarities of phases. Figs 6 and 8 show that SNRs of coherent phases in the processed wavefields are enhanced, which facilitates accurate polarity identification and interpretation. These improvements extend beyond reflection imaging, as there are several applications in seismology where accurate earthquake phase detection is required (e.g. in seismic tomography studies).

7.3 Geological implications and non-uniqueness of identified phases

In Section 6, several coherent phases were identified. Given the good agreement between modelled ghost reflections and real data, it seems reasonable to interpret these arrivals as reflections from the magma pocket at 2.1 km depth at the IDDP1. In that case, the magma body would extend at least from ~ 170 m south to ~ 500 m north of the IDDP1, with a width of at least ~ 200 m, but definite conclusions regarding the size of the reflector cannot be drawn, as bounce points sample only a restricted area at the IDDP1 (Fig. 7a). A larger extent of the magma pocket is suggested by Kim $et\ al.$

(2020), who identified several reflectors in the area of the IDDP1 around the depth where magma was encountered, some extending over 1 km.

However, the arrival time of a phase may correspond to different wave types that follow various paths through the Earth but arrive simultaneously at the receivers. Especially volcanoes are expected to produce a wide range of complex ray paths due to multiple scattering and reflections at heterogeneities and subsurface layers. We illustrate this with a simple example: assuming primary reflections, we use ray tracing and the aforementioned 1-D velocity models to calculate the depth of a reflector that would create a seismic reflection arriving at 2.5 s on the horizontal components. Previously, this arrival was interpreted as a P-S-S ghost reflection (Section 6). We find that either a P-to-S converted wave reflecting at 4.4 km b.s.l. or a pure S-S phase reflecting at 3.7 km b.s.l. would yield an arrival time of 2.5 s on the radial component. Interestingly, several studies suggest the presence of a 2-6 km wide low-velocity body beneath the Krafla caldera, with its upper boundary at approximately 3 km depth and a thickness of 0.75 to 1.8 km (e.g. Einarsson 1978; Brandsdóttir et al. 1997).

Our simple example highlights the need for caution in interpreting seismic phases. Usually, when multiple stations are deployed, the moveout, or the apparent velocity of waves at the receivers can help to discriminate between different wave types. However, in our setting moveouts of waves are very similar due to the limited extent of our study area (Section 3). This complicates phase discrimination based on apparent velocity. In addition to apparent velocity, polarities of phases can help to differentiate between reflected phases. For example, the impedance contrast between the subsurface rock

and air at the free surface results in a negative reflection coefficient for a *P*-wave ghost reflection, causing a polarity reversal and thus an opposite polarity compared to primary reflections.

In addition to the discussed arrivals aligning with modelled ghost reflections, other consistent phases are present in the data (Figs 8 and 9). These phases could correspond to refractions and reflections from various depths, as well as to upper and lower boundaries of geological structures, potentially providing insights into the thickness of the magma pocket. Future investigations will focus on the analysis of phase polarities and on the inversion of additional phases to distinguish reflected phases, strengthen the geological interpretation and gain deeper insights into the subsurface structure at Krafla.

8 CONCLUSION

In this work, we investigated the limitations of passive reflection imaging in complex geological settings and proposed strategies to overcome them. We analysed high-frequency (5–20 Hz) seismic data from over 300 local microearthquakes (M < 1.5) and noise from the geothermal plant, recorded by a dense network of seismic stations at Krafla volcano, NE Iceland. Our findings can be summarized as follows:

- (i) Although clear *P* and *S*-wave onsets are recorded at Krafla for most events, the time-series and spectral characteristics following the *S*-wave arrival lack coherency between closely spaced (30 m) stations. This highlights the main limitation of passive reflection imaging in complex settings: the heterogeneous subsurface and the dominance of site effects in the wavefields.
- (ii) Data are more coherent in the common-station domain, where fixing the station stabilizes the site effect. This allowed us to address, characterize and subsequently reduce the impact of site effects and incoherent scattering in the data. We therefore recommend data analyses in the common-station domain in complex geological settings where site effects strongly influence the wavefields.
- (iii) Site effects are partly due to seismic resonance effects within the heterogeneous near-surface underneath the stations. Through autocorrelation techniques, we constructed transfer functions accounting for these resonances and designed a resonance removal filter that efficiently deconvolves them from the data. We propose the resonance removal filter, which does not rely on *a priori* knowledge of the elastic properties of the subsurface, as an effective method to address near-surface resonance effects in seismic data from volcanoes and other complex media. Linear stacking and nonlinear amplitude weighting are additional techniques that reduce incoherent scattering and enhance the signal-to-noise ratios of coherent phases.
- (iv) We applied our workflow to the area at the IDDP1 borehole at Krafla, where rhyolitic magma was unexpectedly encountered in 2009 during geothermal drilling. The processed data revealed several coherent phases which are possible reflections from the known magma—rock interface at 2.1 km depth.

In future work, we plan to investigate amplitudes and polarities in detail and integrate our workflow with additional imaging methods, in order to deepen our understanding of the Krafla geothermal system.

ACKNOWLEDGMENTS

We thank Christopher Juhlin and one anonymous reviewer for insightful comments that helped to improve the manuscript. RM was funded by the European Union's Horizon 2020 research and innovation programme under the Marie Skłodowska-Curie grant agreement No 858092 - IMPROVE (www.improve-etn.eu). We are grateful to Anette K. Mortensen and Landsvirkjun, the national power company of Iceland, for hosting us during the 2022 Krafla field campaign, providing data, and sharing their knowledge of the Krafla area. We thank Þorbjörg Ágústsdóttir, Egill Árni Guðnason and Iceland GeoSurvey (ÍSOR) for supplying data and expert insights into the Krafla region. Likewise, we thank Philippe Jousset and the researchers from GFZ Potsdam, Section 2.2, as well as Benjamin Schwarz, Jonathan Wolf, Ivan Lokmer, Ziqi Zhang, Tolulope Olugboji and the DIAS geophysics section for fruitful discussions about this research. We also thank Maurice Weber, Elisabeth Glück and other IMPROVE ESRs who assisted with the field work.

DATA AVAILABILITY

Seismic data used in this study were collected during the 2022 IMPROVE field campaign at Krafla and are available on Zenodo (Maass *et al.* 2024). This data set includes (i) the earthquake recorded by profile L1 shown in Fig. 2, (ii) the earthquake traces used to generate the common-station gather in Fig. 3 for station L1013 and (iii) the seventeen earthquakes at the IDDP1 borehole recorded by the 3C stations of profile L2, utilized for imaging in Section 6 (Figs 7–9).

REFERENCES

- Akuhara, T. & Mochizuki, K., 2015. Hydrous state of the subducting Philippine Sea plate inferred from receiver function image using onshore and offshore data, J. geophys. Res.: Solid Earth, 120(12), 8461–8477.
- Aloisi, M., Cocina, O., Neri, G., Orecchio, B. & Privitera, E., 2002. Seismic tomography of the crust underneath the Etna volcano, Sicily, *Phys. Earth planet. Inter.*, 134(3), 139–155.
- Arnott, S.K. & Foulger, G.R., 1994. The Krafla spreading segment, Iceland:

 Three-dimensional crustal structure and the spatial and temporal distribution of local earthquakes, *J. geophys. Res.: Solid Earth*, 99(B12), 23801–23825.
- Backus, M.M., 1959. Water reverberations—Their nature and elimination, *Geophysics*, **24**(2), 233–261.
- Bakulin, A., Ramdani, A., Neklyudov, D. & Silvestrov, I., 2023. Meter-scale geologic heterogeneity in the near surface explains seismic speckle scattering noise, *Leading Edge*, 42(10), 683–694.
- Barison, E., Poletto, F., Böhm, G., Farina, B., Carrasco-Núñez, G., Norini, G., Giordano, G. & Pinna, G., 2023. Processing and interpretation of seismic reflection data from the Los Humeros super-hot geothermal system, *Geothermics*, 113, 102771, doi:10.1016/j.geothermics.2023.102771.
- Bensen, G.D., Ritzwoller, M.H., Barmin, M.P., Levshin, A.L., Lin, F., Moschetti, M.P., Shapiro, N.M. & Yang, Y., 2007. Processing seismic ambient noise data to obtain reliable broad-band surface wave dispersion measurements, *J. geophys. Int.*, 169(3), 1239–1260.
- Björnsson, A., Saemundsson, K., Einarsson, P., Tryggvason, E. & Grönvold, K., 1977. Current 607 rifting episode in north Iceland, *Nature*, 266, 318–323
- Blondel, T., Chaput, J., Derode, A., Campillo, M. & Aubry, A., 2018. Matrix approach of seismic imaging: application to the Erebus volcano, Antarctica, *J. geophys. Res.: Solid Earth*, **123**(12), 10 936–10 950.
- Brandsdóttir, B. & Menke, W.H., 1992. Thin low-velocity zone within the krafla caldera, ne-Iceland attributed to a small magma chamber, *Geophys. Res. Lett.*, 19(24), 2381–2384.
- Brandsdóttir, B., Menke, W., Einarsson, P., White, R.S. & Staples, R.K., 1997. Färoe-Iceland Ridge Experiment 2. Crustal structure of the Krafla central volcano, *J. geophys. Res.: Solid Earth*, **102**(B4), 7867–7886.

- Bruno, P., Maraio, S. & Festa, G., 2017. The shallow structure of Solfatara Volcano, Italy, revealed by dense, wide-aperture seismic profiling, *Sci. Rep.*, 7, 17386, doi:10.1038/s41598-017-17589-3.
- Byerly, K., Brown, L., Voight, B. & Miller, V., 2010. Reflection imaging of deep structure beneath Montserrat using microearthquake sources, *Geophys. Res. Lett.*, **37**(19), doi:10.1029/2009GL041995.
- Cunningham, E. & Lekic, V., 2019. Constraining crustal structure in the presence of sediment: a multiple converted wave approach, *J. geophys.* Int., 219(1), 313–327.
- De Barros, L., Martini, F., Bean, C.J., Garcia-Yeguas, A. & Ibáñez, J., 2012.
 Imaging magma storage below Teide volcano (Tenerife) using scattered seismic wavefields, *J. geophys. Int.*, 191(2), 695–706.
- Dello Iacono, D., Zollo, A., Vassallo, M., Vanorio, T. & Judenherc, S., 2009.
 Seismic images and rock properties of the very shallow structure of Campi Flegrei caldera (southern Italy), *Bull Volcanol*, 71, 275–284.
- Dondurur, D., 2018. Chapter 5 preprocessing, in Acquisition and Processing of Marine Seismic Data, pp. 241–312, ed. Dondurur, D., Elsevier.
- Einarsson, P., 1978. S-wave shadows in the Krafla caldera in NE-Iceland, evidence for a magma chamber in the crust, *Bull. Volcanol.*, **41**(3), 1–9.
- Elders, W.A. et al. 2011. Origin of a rhyolite that intruded a geothermal well while drilling at the Krafla volcano, Iceland, Geology, 39(3), 231–234.
- Fichtner, A., Bowden, D. & Ermert, L., 2020. Optimal processing for seismic noise correlations, J. geophys. Int., 223(3), 1548–1564.
- Giraudat, E., Burtin, A., Le Ber, A., Fink, M., Komorowski, J.-C. & Aubry, A., 2024. Matrix imaging as a tool for high-resolution monitoring of deep volcanic plumbing systems with seismic noise, *Commun. Earth Environ.*, 5(509), doi:10.1038/s43247-024-01659-2.
- Guðnason, E.Á., Magnússon, R.L. & Ágústsdóttir, Þ., 2023. Seismic Monitoring in Krafla, Þeistareykir and Námafjall. Reprocessing of the Entire 2006–2022 Catalogue., Report no. LV-2023-021. Prepared by Iceland GeoSurvey (ÍSOR) for Landsvirkjun (LV).
- Jaxybulatov, K., Koulakov, I., von Seht, M.I., Klinge, K., Reichert, C., Dahren, B. & Troll, V.R., 2011. Evidence for high fluid/melt content beneath Krakatau volcano (Indonesia) from local earthquake tomography, J. Volc. Geotherm. Res., 206(3), 96–105.
- Kim, D., Brown, L.D., Árnason, K., Águstsson, K. & Blanck, H., 2017.
 Magma reflection imaging in Krafla, Iceland, using microearthquake sources, J. geophys. Res.: Solid Earth, 122(7), 5228–5242.
- Kim, D., Brown, L.D., Árnason, K., Gudmundsson, Ó., Ágústsson, K. & Ólafur, G.F., 2020. Magma "bright spots" mapped beneath Krafla, Iceland, using RVSP imaging of reflected waves from microearthquakes, *J. Volc. Geotherm. Res.*, 391, 106365, doi:1016/j.jvolgeores.2018.04.022.
- Konno, K. & Ohmachi, T., 1998. Ground-motion characteristics estimated from spectral ratio between horizontal and vertical components of microtremor, *Bull. seism. Soc. Am.*, 88(1), 228–241.
- Liu, Y.-W., 2012. Hilbert Transform and Applications, in Fourier Transform, chap. 12, ed. Salih, S.M., IntechOpen.
- Maass, R., Li, K.L. & Bean, C.J., 2024. Seismic data used in 'Improving passive reflection seismic imaging in complex geological settings through site effect reduction: application to Krafla volcano, Iceland.' [Data set] Zenodo, https://doi.org/10.5281/zenodo.14531615
- Margrave, G.F., 2000. New seismic modelling facilities in Matlab. https://api.semanticscholar.org/CorpusID:61465960
- Martini, F. & Bean, C.J., 2002. Interface scattering versus body scattering in subbasalt imaging and application of prestack wave equation datuming, *Geophysics*, 67(5), 1593–1601.
- Matsumoto, S. & Hasegawa, A., 1996. Distinct S wave reflector in the midcrust beneath Nikko-Shirane volcano in the northeastern Japan arc, J. geophys. Res.: Solid Earth, 101(B2), 3067–3083.
- Matsumoto, S., Shimizu, H., Onishi, M. & Uehira, K., 2012. Seismic reflection survey of the crustal structure beneath Unzen volcano, Kyushu, Japan., *Earth Planet Sp*, 64, 405–414.
- Mortensen, A., Grönvold, K., Guðmundsson, Á., Steingrímsson, B. & Egilson, Þ., 2010. Quenched Silicic Glass from Well KJ-39 in Krafla,

- North-Eastern Iceland, in *Proceedings World Geothermal Congress 2010*, World Geothermal Congress 2010, Bali, Indonesia.
- Mortensen, A., Egilson, P., Gautason, B., Árnadóttir, S. & Guðmundsson, Á. 2014. Stratigraphy, alteration mineralogy, permeability and temperature conditions of well IDDP-1, Krafla, NE-Iceland, *Geothermics*, 49, 31–41.
- Obermann, A., Lupi, M., Mordret, A., Jakobsdóttir, S.S. & Miller, S.A., 2016. 3D-ambient noise Rayleigh wave tomography of Snæfellsjökull volcano, Iceland, J. Volc. Geotherm. Res., 317, 42–52.
- O'Brien, G.S. & Bean, C.J., 2009. Volcano topography, structure and intrinsic attenuation: their relative influences on a simulated 3D visco-elastic wavefield, *J. Volc. Geotherm. Res.*, 183(1), 122–136.
- Okaya, D.A., 1995. Spectral properties of the Earth's contribution to seismic resolution, *Geophysics*, **60**(1), 241–251.
- Onacha, S., Kahn, D., Malin, P. & Shalev, E., 2005. Resistivity and microearthquake imaging of Krafla geothermal field, NE Iceland, *Trans.—Geotherm. Resources Council*, 29, 497–502.
- Pavez, C., Comte, D., Gutiérrez, F. & Gaytán, D., 2019. Analysis of the magmatic–hydrothermal volcanic field of Tacora volcano, northern Chile using travel time tomography, J. South Am. Earth Sci., 94, 102247, doi:10.1016/j.jsames.2019.102247.
- Rezaeifar, M., Bean, C.J., Grannell, J., Möllhoff, M. & Bell, A.F., 2024. Intrusive mechanism of the 2018 Sierra Negra Galápagos eruption, constrained by 4D tomographic images, *J. Volc. Geotherm. Res.*, **451**, 108112, doi:10.1016/j.jvolgeores.2024.108112.
- Schuler, J. et al. 2015. Seismic imaging of the shallow crust beneath the Krafla central volcano, NE Iceland, J. geophys. Res.: Solid Earth, 120(10), 7156–7173.
- Sheriff, R.E., 1977. Limitations on Resolution of Seismic Reflections and Geologic Detail Derivable from Them1, in *Seismic Stratigraphy— Applications to Hydrocarbon Exploration*, ed. Payton, C.E., American Association of Petroleum Geologists.
- Stankiewicz, J., Ryberg, T., Haberland, C., Fauzi, & Natawidjaja, D., 2010.
 Lake Toba volcano magma chamber imaged by ambient seismic noise tomography, *Geophys. Res. Lett.*, 37(17), doi:10.1029/2010GL044211.
- Tauzin, B., Pham, T.-S. & Tkalčić, H., 2019. Receiver functions from seismic interferometry: a practical guide, J. geophys. Int., 217(1), 1–24
- Thore, P.D. & Juliard, C., 1999. Fresnel zone effect on seismic velocity resolution, *Geophysics*, **64**(2), 593–603.
- Thurber, C.H., Li, Y. & Johnson, C., 1989. Seismic detection of a low-velocity layer beneath the southeast flank of Mauna Loa, Hawaii, *Geophys. Res. Lett.*, **16**(7), 649–652.
- Tryggvason, E., 1994. Surface deformation at the Krafla volcano, North Iceland, 1982–1992., Bull. Volcanol., 56, 98–107.
- Urra-Tapia, P., González-Vidal, D., Miller, M. & Palma, J.L., 2023.
 The seismic structure of Villarrica Volcano revealed by ambient noise tomography, *J. Volc. Geotherm. Res.*, 439, 107829, doi:10.1016/j.jvolgeores.2023.107829.
- Weemstra, C., Westra, W., Snieder, R. & Boschi, L., 2014. On estimating attenuation from the amplitude of the spectrally whitened ambient seismic field, *J. geophys. Int.*, 197(3), 1770–1788.
- Yilmaz, O., 2001. Seismic Data Analysis: Processing, Inversion, and Interpretation of Seismic Data [Volume I], pp. 1028, ed. Doherty, S.M., Society of Exploration Geophysicists.
- Yu, Y., Song, J., Liu, K.H. & Gao, S.S., 2015. Determining crustal structure beneath seismic stations overlying a low-velocity sedimentary layer using receiver functions, *J. geophys. Res.: Solid Earth*, 120(5), 3208–3218.
- Zhang, Z. & Olugboji, T., 2021. The signature and elimination of sediment reverberations on submarine receiver functions, J. geophys. Res.: Solid Earth, 126(5), e2020JB021567, doi:10.1029/2020JB021567.
- Zhang, Z. & Olugboji, T., 2023. Lithospheric imaging through reverberant layers: sediments, oceans, and glaciers, *J. geophys. Res.: Solid Earth*, **128**(5), e2022JB026348, doi:10.1029/2022JB026348.